5

MEMS Characterization Based on Optical Measuring Methods

Tong Guo[1], Long Ma[2] and Yan Bian[3]
[1]*Tianjin University*
[2]*Civil Aviation University of China*
[3]*Tianjin University of Technology and Education*
P.R. China

1. Introduction

Micro Electro Mechanical Systems (MEMS) is developed based on the semi-conductor technology, however, relative material, design, fabrication, simulation, packaging and test are more complex than those in semi-conductor technology. In the primary stage, MEMS technology focused on the design and development, now on the commercialization and improving reliability and decreasing cost and price. So test is increasingly important to MEMS technology and testing cost is about 1/3 of the whole cost of MEMS. In order to improve the production and decrease the cost, producers and researchers pay more attention to MEMS test to solve all the testing problems from design to packaging process.
There are a number of methods to carry out these measurements, such as scanning electron microscopy (SEM), atomic force microscopy (AFM), stylus profiler, and optical profiler, etc. Every method has its advantages and disadvantages.

- SEM is one of the most common measurement tools. However, nearly all nonconductive specimens examined using SEM need to be coated with a thin film of conducting material. This may result in bending or distortion of the device, especially where free structures such as cantilever beams. SEM tests are also time consuming and not suitable for a production environment.
- AFM has been suggested as a MEMS measurement tool. As with SEM, analysis may be slow (about 20 min/device), and the limited measurement range of an AFM (100 μm×100 μm×5 μm, Veeco multimode AFM) means that it is unable to investigate large samples or out-of-plane devices such as the cantilevers. It is also difficult to examine packaged devices using an AFM.
- Mechanical stylus surface profilers are commonly used for dimensional measurements in MEMS. While these can measure step heights with a high accuracy, they are not suitable for the analysis of freestanding structures, where the stylus may break the device under test. Deep, high aspect ratio devices also pose problems, as the stylus probe may be too large to accurately reproduce the surface profile.

If MEMS devices need to fit the large-scale production, it is essential that these measurements must be cheaply and easily made at the wafer level, without the need for large space, expensive packaging or destructive test methods. Optical techniques can offer

solutions to many of these problems. This chapter uses computer micro-vision and microscopic interferometry to carry out MEMS measurements, including dimensional (static) and moving (dynamic) properties analysis. The moving properties can be classified into in-plane (lateral) movements and out-of-plane (vertical) movements. The techniques involved are simple, fast, non-destructive, requiring no sample preparation and may be carried out at wafer level - all important requirements for high volume production.

2. System set-up

2.1 Microscopic interferometer

The interferometer is the device which can generate the interferogram patterns. The typical microscopic interferometers used in MEMS measurement include Michelson-type, Mirau-type and Linnik-type. The scheme of optical structures in these interferometers is shown in figure 1.

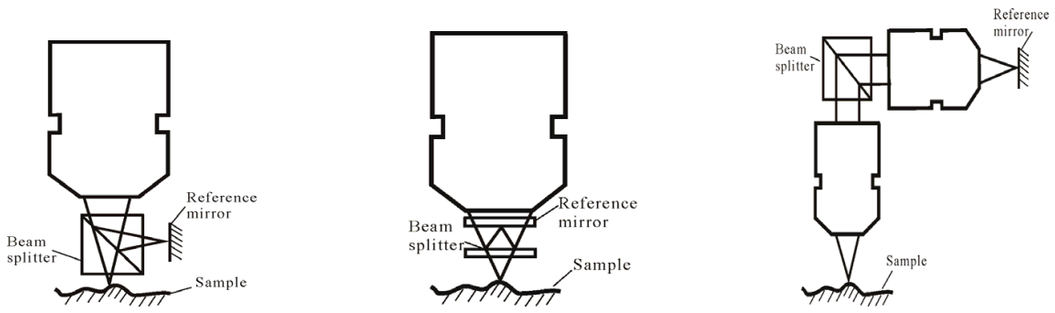

(a) Michelson interferometer (b) Mirau interferometer (c) Linnik interferometer

Fig. 1. Schematic layout of the three types of interferometers

Inside the interferometer the light is divided into two beams, one beam is guided on the sample surface as the test beam, and the other one goes to the reference mirror as the reference beam. When the OPD is within the coherence length, the reflected test beam and reference beam will interfere with each other and produce interference fringe patterns. Figure 1(a) presents the Michelson interferometer, where a beam splitter is placed in front of the objective. Hence, the working distance of the objective must be relatively large which makes the magnification of Michelson interferometer the lowest of the three types of interferometers shown in figure 1. Figure 1 (b) is the Mirau interferometer, which is widely equipped in lots of commercial optical profilers. Inside this interferometer, the light is split by a very thin and flat optical mirror. As result, the mechanical structure of this interferometer is more compact than that of Michelson type. Besides, the light path between the test beam and the reference beam is very similar, which can also minimize optical disturbance. Figure 1 (c) illustrates the layout of the Linnik interferometer, from where one can see the beam splitter is located behind the objective. Therefore, Linnik interferometer can use the objective with shorter working distance and higher magnification. However, the unconformity between the two objectives may cause measurement errors, and that is why in the application of Linnik interferometer the two objectives must be matched very well.

2.2 Measurement system

Two sets of measurement systems were developed in our laboratory. The first one is for static characterization, the other one is for dynamic characterization.

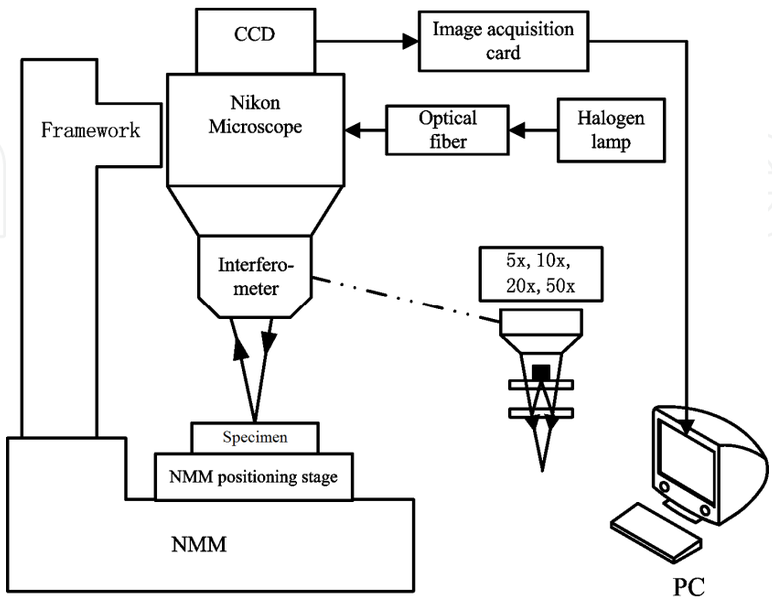

Fig. 2. Scheme of the static characterization system

As a foundation of our system, the nano-measuring machine (NMM) was used, which was developed in Ilmenau University of Technology of Germany for surface measurement within a measuring volume of 25mm×25mm×5mm. Three commercial interferometers inside the NMM read the stage position in real time so that the positioning control loop can assure a movement resolution of 0.1 nm. The sensor arrangement provides an Abbe error-free measurement on all three NMM axes. Based on the NMM, various measuring systems could be integrated.

The layout of the first experimental system used in this context is illustrated in figure 2. To increase the optical system robustness, we chose a commercial interferometer system with halogen lamp fibre illumination from NIKON. A CCD camera recorded the interferogram at equidistant positions and transfered them into a computer for data processing. In the laboratory, the system was assembled inside a cover where a vibration isolation table was provided. Additionally, in order to further decrease the influence of vibrations, we placed the entire equipment on a special independent foundation.

The second system is called micro motion analyzer (MMA). The structure of MMA is shown in figure 3. MMA was equipped with several long working distance optical objectives from Zeiss company, including 5×, 10×, 20× and 50×. There were two kinds of light sources: one was a high performance LED (Nichia NSPG 500S LED, central wavelength was 525nm, optical bandwidth was 40nm) to be used in the in-plane motion measurement; the other was a LD (Hitachi HL6501MG, the power was 50mW, the wavelength was 658nm) to be used in the out-of-plane motion measurement. A nano-positioner (PI P-721.CL, capacitor sensor feedback control in close loop) was used to shift the phase of the interferogram and adjust the optical path with sub-nanometer resolution. The bright field and interference field were switched by putting a stop plate in the reference optical path. Images were captured by a

digital CCD camera (Microvision, 1280×1024 pixels, 9μm pixel distance, 100% filling factor, 10 bits grayscale resolution), then transferred to the server to be post-processed. The user can transfer and receive instructions and data through TCP/IP protocol on a client PC. The system was also equipped with a signal generating unit and a high voltage amplifying unit to output high voltage signal and stimulate the tested MEMS device. The system was placed on a vibration isolation table (TMC Lab Table) to decrease the effect of outside vibration. The system was also equipped with a probe station (Karl Suss, Germany) to test the unpackaged MEMS devices. Here digital phase lock loop (PLL) made the stimulating signal, illuminating signal and the image capturing synchronized. The frequency range of Arbitrary Waveform Generator (AWG) was from 1 Hz to 10 MHz, and the sampling frequency was 40 MHz.

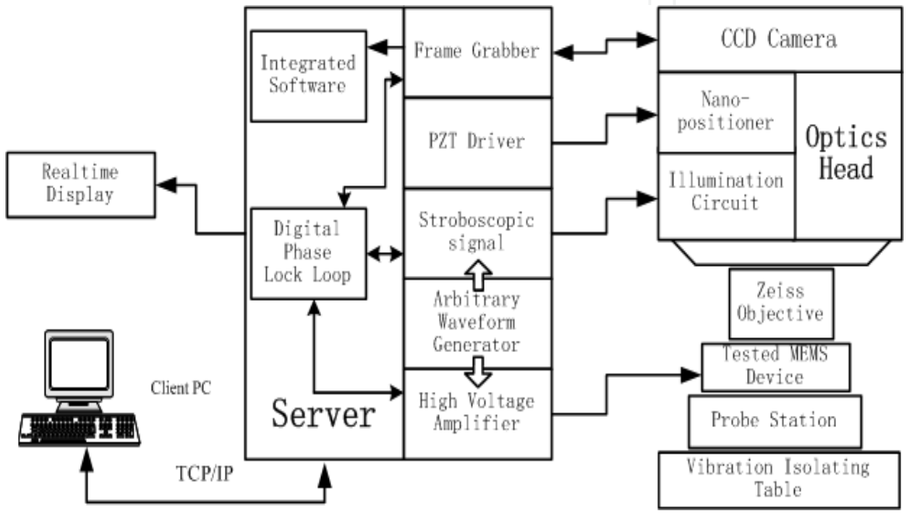

Fig. 3. Structure diagram of the MMA

3. Measurement principles

3.1 Static characterization

Static characterization is a very important aspect in MEMS technology, especially for the design and manufacture of micro- or nano-sensors and actuators. In general case, the goal of static characterization is to derive the geometrical parameters, such as surface topography, profile, waviness, roughness and depth-width ratio, etc.

3.1.1 Phase-shifting interferometry (PSI)

If we denote the coordinates in the plane of the CCD array as (x, y), we can write the intensity of the interference pattern I(x, y) as:

$$I(x,y) = A(x,y) + B(x,y)\cos[\phi(x,y) + \varphi] \tag{1}$$

Where $A(x, y)$ is the function representing the mean background intensity of the interferogram; $B(x, y)$ is the function determining the modulation of the interferogram; $\phi(x, y)$ is the function dependent on the unwrapped phase $\theta(x, y)$ which represents the height change on the sample; phase φ is a constant, which can be adjusted by changing the position in the axial direction between the objective and the sample.

Using a series of I measured at different phase φ value, Hariharan phase-shifting algorithm is used to extract height information on devices' surface in I. The intensities are I_1, I_2, I_3, I_4 and I_5 respectively. The formula of calculating wrapped phase ϕ is as follows.

$$\phi(x,y) = \arctan\left[\frac{2(I_2 - I_4)}{2I_3 - I_1 - I_5}\right] \tag{2}$$

This algorithm need change π/2 between two successive image capturing. This algorithm is repressive to the calibration error of the phase-shifter and the nonlinear errors of the detector, so it improves the measurement accuracy.

Measurements using single-wavelength interferometry have an inherent 2π phase ambiguity, which means phase maps must be unwrapped by removing artificial 2π jumps before they can be properly interpreted in terms of surface height. This process is called phase unwrapping. Now there are many kinds of phase unwrapping algorithms. In the experiments, considering about the testing speed and the real quality of the interferogram, quality-guided path following algorithm is used to retrieve the actual phase map. The surface height can be calculated by the following formula.

$$h = \frac{\theta}{4\pi}\lambda \tag{3}$$

Here, λ is the wavelength of the light source.

Figure 4 shows the wrapped phase map and the unwrapped map in the process of dealing with the captured images. The tested sample is a membrane.

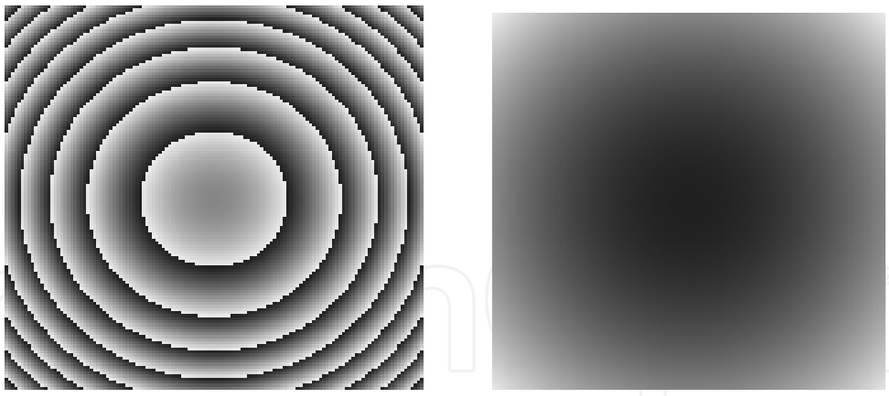

(a) Wrapped phase map (b) Unwrapped phase map

Fig. 4. Pictures of processed results

3.1.2 White light scanning interferometry (WLI)

PSI is widely used to test smooth surfaces and is very accurate, resulting in vertical measurements with sub-nanometer resolution. However, PSI cannot obtain a correct profile for objects that have large step changes because it becomes ineffective as height discontinuities of adjacent pixels exceed one quarter of the used wavelength (λ/4), which is also called "phase ambiguity".

White light scanning interferometry (WLI) provides a good solution to overcome "phase ambiguity". Here we track point P and Q in figure 5 to illustrate the scan process of WLI. When Q stays outside the coherence length of the light source, the intensity detected is nearly the same with the background irradiance, corresponding to t_1 to t_2. Afterwards, from time t_2 when Q starts to move into the coherence length zone, the signals extracted of point Q will be kept modulating by the interferogram until it travels out at t_5. During the scan, the maximum visibility will occur at t_4 where the testing beam matches the reference beam. The above process is roughly similarity for point P. Once retrieved the correlogram, the peak position of the intensities can then be used as an indicator of the surface relative height.

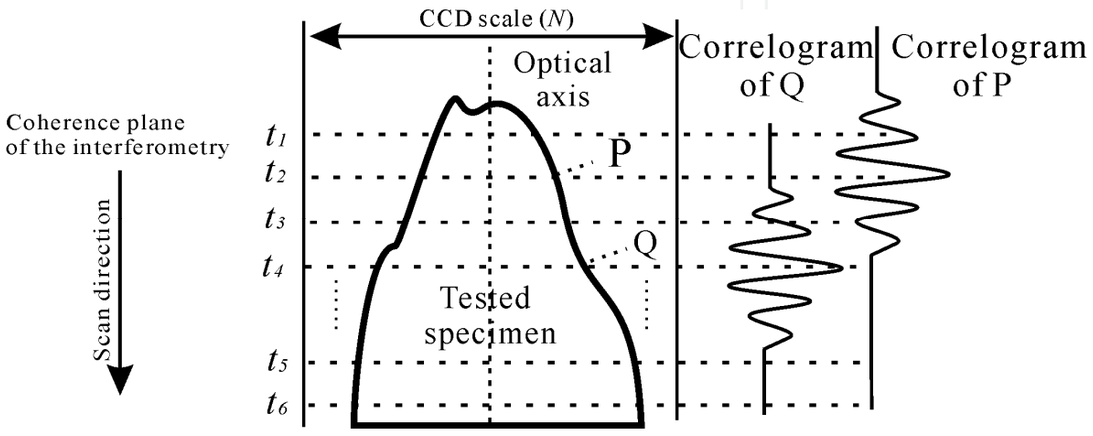

Fig. 5. Schematic diagram of white light vertical scanning interferometry

The white light correlogram recorded by the CCD camera in the white light interferometry can be expressed as:

$$I = I_0\left[1 + \gamma g(z)\cos(\phi + \alpha)\right] \tag{4}$$

Where I is the measured intensity, I_0 is the background irradiance value, γ is a constant, $g(z)$ is the fringe visibility in the form of Gaussian function, ϕ is the phase value depended on the optical path difference and the α is the additional phase term due to different reflections. Generally, the maximum location of $g(z)$ is usually extracted for the height evaluation. This process can be done either in spatial space or in frequency domain.

So far, the white light signal demodulation techniques can be basically categorized into two main groups: spatial domain algorithms and frequency domain algorithms. The first group consists of polynomial interpolation, centroid method and Hilbert transform, whereas the latter has Fourier transform, wavelet transform and spatial frequency domain analysis, etc. In general case, algorithms from the second group can perform the surface characterization with a higher resolution. Nevertheless, because of the transform procedures from the spatial domain to frequency domain (various types of convolutions), the second group algorithms are usually time consuming; on the contrary, the first group is efficient but with lower resolution. The other methods are generally based upon the above algorithms and will not be mentioned here.

3.1.3 White light phase-shifting interferometry (WLPSI)

3.1.3.1 Phase extraction

Carré proposed a new phase shifting interferometry in 1966. Unlike the conventional PSI, Carré's method does not require several fixed phase steps (for example, λ/8), but only equal ones, which makes it much easier for most PZTs to fulfill. Suppose the phase step is set to be 2δ, Carré's method can be expressed as:

$$I_1(x,y) = I_0\{1+\gamma\cos[\phi(x,y)-3\delta]\} \tag{5}$$

$$I_2(x,y) = I_0\{1+\gamma\cos[\phi(x,y)-\delta]\} \tag{6}$$

$$I_3(x,y) = I_0\{1+\gamma\cos[\phi(x,y)+\delta]\} \tag{7}$$

$$I_4(x,y) = I_0\{1+\gamma\cos[\phi(x,y)+3\delta]\} \tag{8}$$

Where I_1 to I_4 are the recorded intensities, I_0 is the background irradiance, γ is a constant indicated the visibility and ϕ is the phase term needed to be extracted.
Then the phase term ϕ can be computed as:

$$\phi = tg^{-1}\frac{\sqrt{|[(I_1-I_4)+(I_2-I_3)][3(I_2-I_3)-(I_1-I_4)]|}}{|[(I_2+I_3)-(I_1+I_4)]|} \tag{9}$$

Here ϕ falls within (-π, +π] and the surface information can be written as:

$$h = \frac{\bar{\phi}}{4\pi}\lambda \tag{10}$$

Where h is the relative height of the surface, $\bar{\phi}$ is the unwrapped phase term, λ is the wavelength used. The relative heights on every point together can then give a surface 3D map of the tested sample.
However, in the white light correlogram, the existence of $g(z)$ will make g be a function of the spatial position along the scanning direction, which means error occurs when we employ the Carré method to carry out the phase computation from a white light interferogram. In the next, we will use computer simulation to study how much this kind of error affects the measuring accuracy.
The generated discrete white light signal $I(n)$ is as follows:

$$I(n) = 200 + 200\exp\{-\frac{[(n-20)\times\Delta]^2}{\sigma^2}\}\cos[\frac{4\pi}{\lambda}(n-20)\times\Delta+\frac{\pi}{7}] \tag{11}$$

Where Δ is the scanning step 60 nm, σ is set to be 500 nm($\sigma=l_c/2\pi$, l_c is the coherence length of the light source), the additional phase term due to different reflections is set to be π/7. Figure 6 is the phase computation simulation, which indicates that: phase extraction error owing to the visibility variety is minimum at the position of the coherence peak; on the other hand, the phase error has a trend of becoming bigger while the phase position travels away from the centre. The minimum phase error is less than 0.02 rad and the equivalent measurement error is smaller than $\lambda/500$. Assumed the wavelength is 600 nm, this error

could be about 1nm and is negligible in comparison with the environment disturbance. This can be explained as the weak modulation effect of the Gaussian function around the zero order fringe of the white light signal, where the value of the Gaussian function can be treated as 1(for normalized Gaussian function).

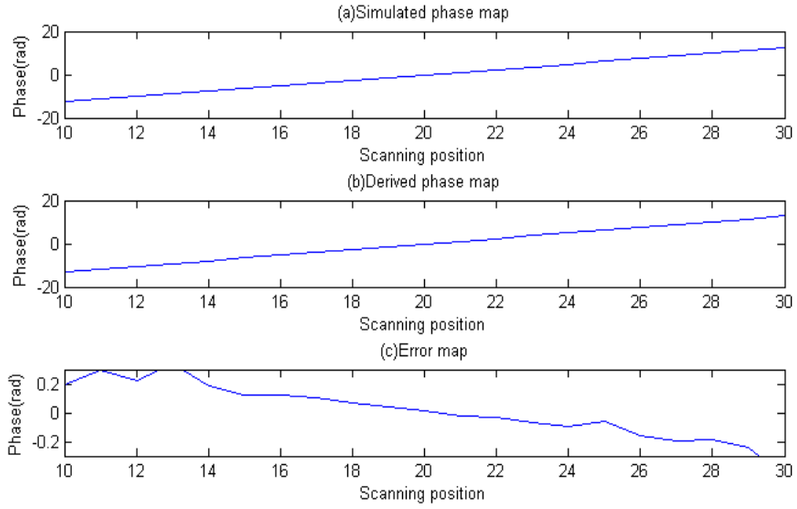

Fig. 6. Phase extraction simulation

3.1.3.2 Height evaluation

Based on the phase computation simulation, the relative height of the tested profile h can then be determined as:

$$h = (stepnumber - peakstep) \times \Delta - t \times [\frac{(\phi + 2k\pi)}{4\pi} \lambda] \tag{12}$$

Where *stepnumber* is the scanning numbers, *peakstep* corresponds to the phase term which comes out of Carré method, Δ is the scanning step and t is the NA parameter. Concerning the NA parameter, both Katherine Creath and C.J.R.Sheppard have given lots of detailed research on the relationship between the objective NA and the fringe width. Here we take this relationship into account and use the results from Ingelstam's equation to calculate this parameter.

$$t = 1 + \frac{(NA_{eff})^2}{4} \tag{13}$$

Where NA_{eff} is the effective numerical aperture.

3.2 Dynamic characterization

The MMA is a highly integrated video microscope, using stroboscopic techniques to capture images of small, fast moving targets. The MMA uses both bright field and interference field based illumination modes combined with sophisticated machine vision algorithms to quantify micro motions. The MMA server and optics head combine the video microscopy with interferometry. However, successful measurements demand several characteristics in

the target. The MMA needs two things: a target that can be moved in a periodic manner, and a target whose video image has contrast or structure when illuminated.

3.2.1 In-plane motion measurement using video microscopy

The MMA calculates the motion of a selected region in a sequence of images using machine vision algorithms. The MMA algorithms are hybrids constructed from a broad class of algorithms (gradient based) that exploit changes in brightness (grayscale values) between images and are capable of measuring motions smaller than the individual pixel size.
Fast moving targets appear blurry. One way of looking at fast moving targets is to slow down their apparent motion using a strobed light source. The scheme shown in figure 7 outlines how carefully timed pulses of light can capture snapshots (samples) of an object motion. These snapshots or images can then be used to reconstruct the displacement trajectory of the target. This is the case for displacements in the focal plane of the microscope or for displacements along the optical axis. It turns out that sometimes different types of images are better for measuring different types of displacements. The MMA optics module provides illumination for two types of images, both of which are acquired in a similar manner.

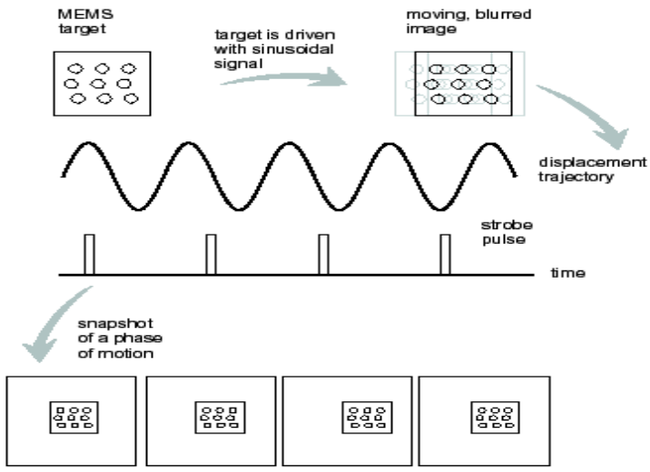

Fig. 7. Freezing rapid movement by stroboscopic illumination

3.2.1.1 Bright field image

By shining a monochromatic incoherent beam of light through the objective lens and uniformily illuminating the target, a bright field image is produced. This is the familiar view through the microscope eyepiece. A bright field image of a MEMS device is shown in figure 8(a).
Optical flow is used to describe the measured motion of brightness patterns between images. The algorithms used by the MMA are optical flow algorithms and are based on two important assumptions or constraints: 1) The brightness of a target region is constant over time, 2) The target region moves as a rigid body.
Motion of the target modulates brightness in the image. The image of a MEMS target moves across an array of pixels. The position of the image is shown at two consecutive timesteps and the registers at the bottom of each image represent the nominal brightness of the corresponding pixel in row 6 (in figure 9). Even sub-pixel motion has measureably changed the brightness in the pixels.

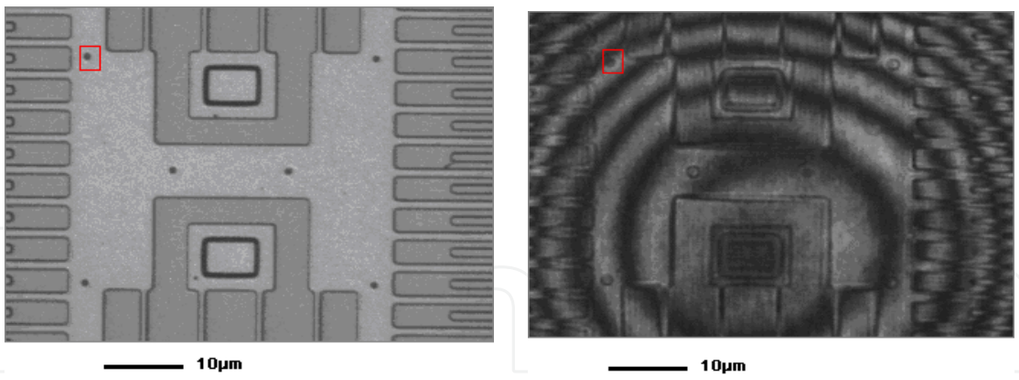

(a) Bright field image (b) Interferometric field image

Fig. 8. Images of the tested micro-resonator

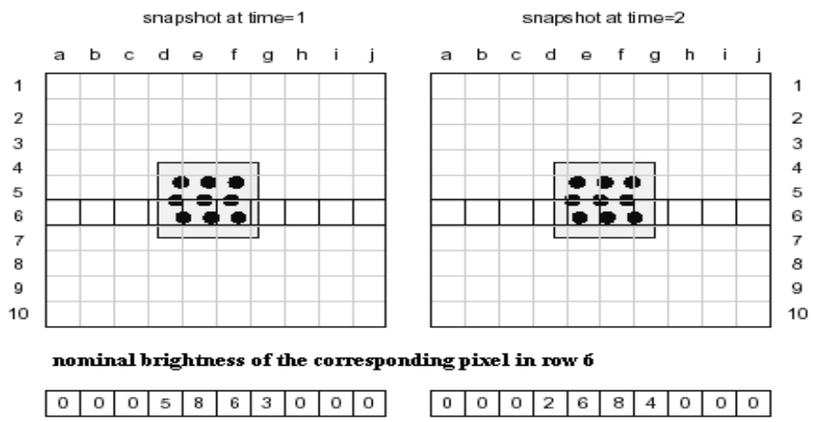

Fig. 9. In-plane motion measurement using optical flow algorithm

The optical flow algorithms used by the MMA work for in-plane or out-of-plane measurements. For out-of-plane measurements, image sequences can be collected at different planes of focus (optical sectioning). In this way, brightness gradients can be sampled along the optical axis and then used in a manner identical to in-plane sequences.

3.2.1.2 Interference field image

Figure 8(b) is the interference field image, which is formed by the reflected light from the tested sample and the reference mirror in the optics module. The interferogram in the picture is sensitive to the optical path change of the sample, which can be used to calculate the height of the sample and the out-of-plane motion between images.

3.2.2 Sub-pixel displacements measurement

The final result of the computation is an extremely powerful tool capable of measuring motions of magnified targets well below the resolution of human vision. Although, the resolution of a single static image is limited in a theoretical sense by the wavelength of the light used to generate the image, the resolution of a motion measurement is limited by the sensitivity of the CCD camera as shown in figure 9. Sub-pixel motion of an object or region

(larger than a pixel) can be measured by using the modulation of the brightness of relevant pixels. It is also clear from figure 9 that changes in the measured brightness can be produced by factors other than motion of the target such as noise in the CCD camera's electronics or fluctuations in the illumination intensity.

3.2.3 Qualifying displacements

In order to quantify in-plane or out-of-plane displacements, the algorithms need a length scale. It means that different measurements need corresponding length scale.

For bright field images (in-plane measurements and optical sectioning), an in-plane length standard such as a grating (a target with a ruling of known spacing) is used to calibrate the length per pixel for a given magnification. The algorithms then convert the calculated displacements from pixels to micrometers.

Interference images have a more convenient length scale available. In this case, measurements are quantified using the known wavelength of the illumination source. This length standard is independent of magnification.

3.2.4 Noise floor analysis

After the data acquisition process is finished, the stimulating system is turned off and the measurement is done again. These two kinds of data are analyzed using the same processing method. Then repeating it five times, the noise floor is described by the RMS value.

4. Experimental results

4.1 Step structure measurement

4.1.1 10 μm standard step height measurement

A 10 μm standard step height fabricated by VLSI (9.976 μm+0.028 μm) was measured, as shown in figure 10, the mean height is 9.984 μm, while the standard deviation is 0.010 μm. The result comparison was presented in figure 11. We can clearly see the step height derived from WLPSI stays in the middle of all the results. Since the algorithms from the second group can achieve higher measurement resolution, the WLPSI can improve the measurement resolution compared with that of the algorithms from the first group.

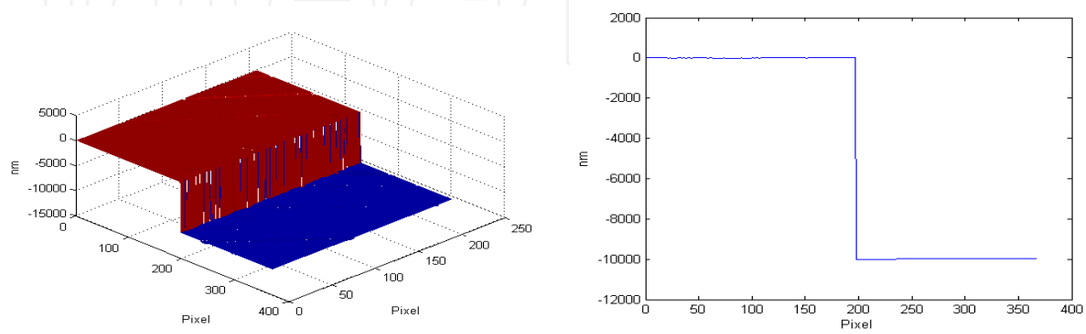

(a) 3D structure (b) Profile

Fig. 10. Measurement of the 10 μm standard step height

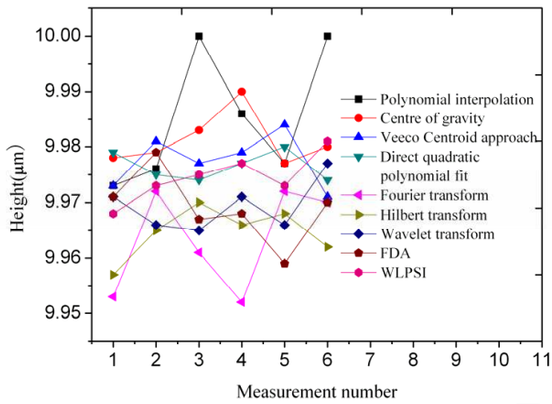

Fig. 11. 10 μm standard step height measurement comparison

4.1.2 44 nm standard step height measurement

Many coherence peak detecting algorithms in white light interferometry perform the height evaluations through either recovering the envelop function or locating the centroid of the correlogram. It works quite well for most surfaces, however, when it comes to some step height alike structures that lower than the coherence length of the illuminator, overshoot will be observed at these discontinuities. This overshoot is also known as batwings, which comes out in form of the high frequency information in the measurement results. Normally, the larger magnification objective always has the higher cutoff spatial frequency, so it will also bring stronger batwings. The batwings is shown in figure 12, where a 44 nm standard step height manufactured by VLSI (43.2 nm±0.6 nm) was measured by Fourier transform.

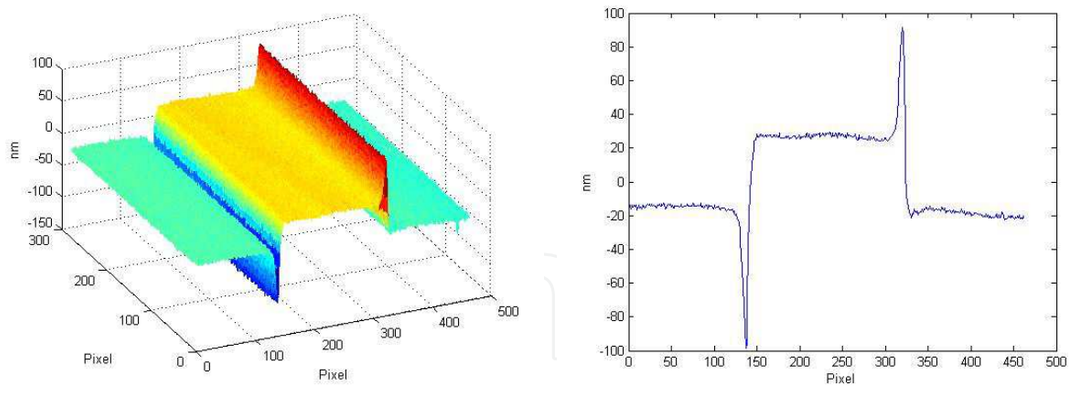

(a) 3D structure of the batwings (b) Profile of the batwings

Fig. 12. Measurement of the 44 nm standard step height with batwings

During the vertical scanning, on condition that the step discontinuities is lower than the coherence length, the light diffracted by the top edge and the light reflected from the bottom will interfere with each other and then travel back to the interferometer. It is because of this diffraction that deforms the correlogram and produces batwings. However, the batwings never occurred in PSI measurements, which gives us a clue to find out the solution for this problem: intensities are much easier to be affected than the phase information in the white

light signals. In this work, we repeated the measurements with WLPSI on the above 44 nm standard step height in figure 12. As illustrated in figure 13, it gave out correct results without batwings.

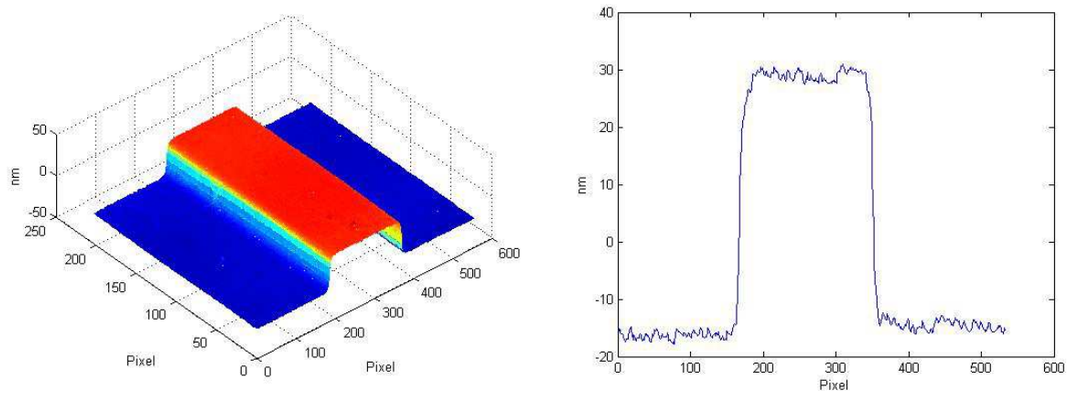

(a) 3D structure (b) Profile

Fig. 13. Measurement of the 44 nm standard step height with WLPSI

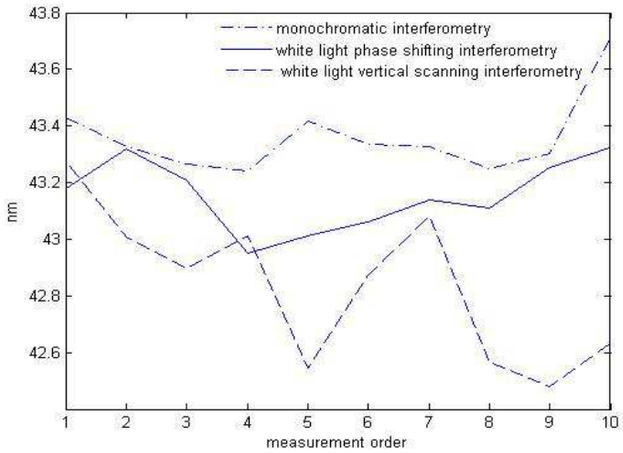

Fig. 14. Comparison of the results from the 44 nm standard step height calibrations

	PSI	WLPSI	WLI
Mean height(nm)	43.36	43.16	42.84
Standard deviation(nm)	0.14	0.13	0.27

Table 1. Measurement results of the 44 nm standard step height using different methods

Figure 14 and table 1 show the 44 nm standard step height evaluations comparison between PSI, WLPSI and WLI. We can clearly see that the results from WLPSI ended up basically in the middle of these three methods and it is close to the results from PSI, which also shows the ability of WLPSI in improving the measurement accuracy compared with the traditional WLI.

4.2 Micro pressure sensor measurement

Experiments were done on a micro pressure sensor using PSI under the air condition. From figure 15(a), a deformed membrane can be seen to show the air pressure. The deform value shows the change of the pressure. From figure 15(b), the height difference between the highest position and the lowest position is 1345.7 nm, which is matched with the designed value.

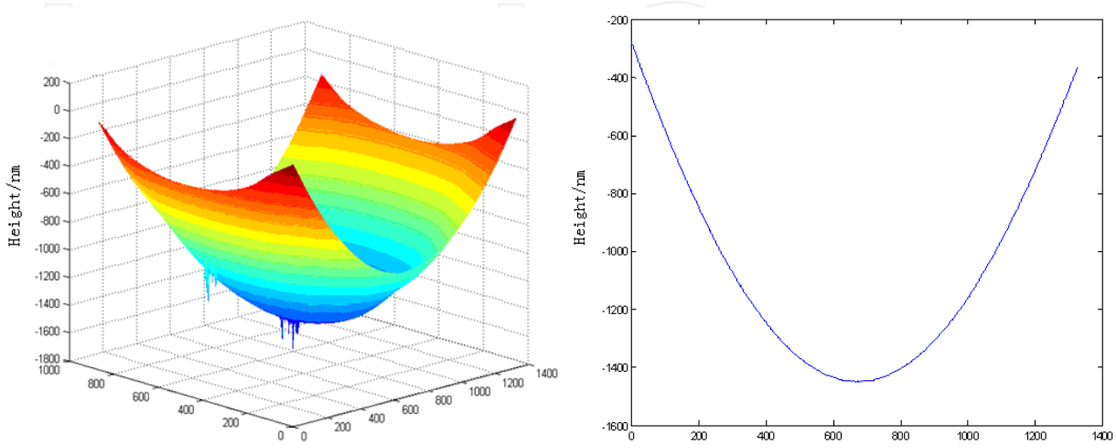

(a) 3D display (b) profile

Fig. 15. Results of micro pressure sensor measurement

4.3 Film structure measurement

Combining with Otsu method from image segmentation technique, we measured a film thickness standard in WLI measurement (centre average thickness: 1052.2 nm±0.9 nm, refraction index: 1.46, model number: FTS4-10100, VLSI) which was calibrated by an ellipsometer in 632.8 nm wavelength. The system equipped 10× Mirau objective to perform a set of repeated measurements". The thickness and the surface topography were successfully extracted, which were shown in table 2 and figure 16. The R_a values of the upper and lower surfaces were 7.30 nm and 7.32 nm, respectively.

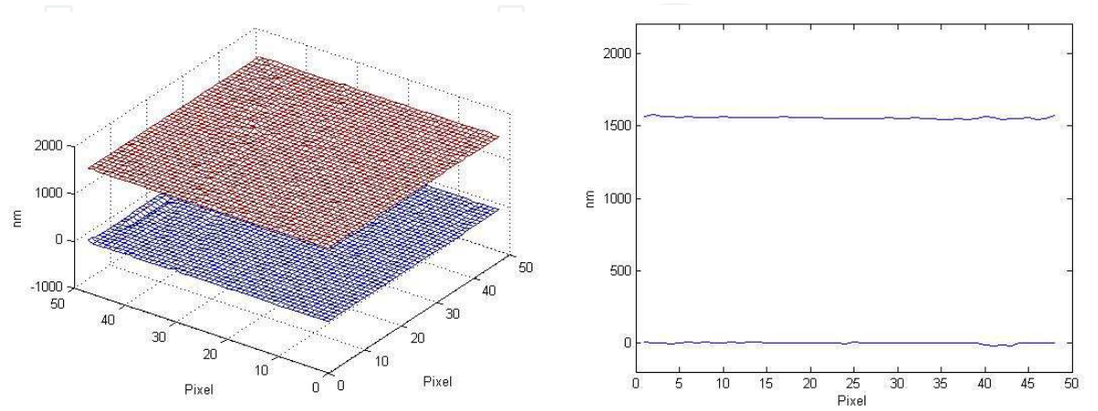

(a) 3D structure (b) Profile

Fig. 16. Film thickness standard measurement

No.	Thickness(nm)	No.	Thickness(nm)	Mean value(nm)	Standard deviation(nm)
1	1053.1	6	1050.9		
2	1053.1	7	1052.3		
3	1050.0	8	1052.1	1051.8	1.43
4	1048.8	9	1052.1		
5	1050.9	10	1053.1		

Table 2. Measurements on film thickness standard

4.4 Micro-resonator measurement

With WLPSI, a micro resonator manufactured by Microelectronics Center of North Carolina (MCNC) was measured. With a 20× Mirau objective, the micro resonator was illuminated by a white light illuminator (central wavelength is 600 nm), the scanning range was configured to be 9 μm and the scanning step was 45 nm. The result is shown in figure 17. The height of the comb-finger profile is approximately 3.8 μm.

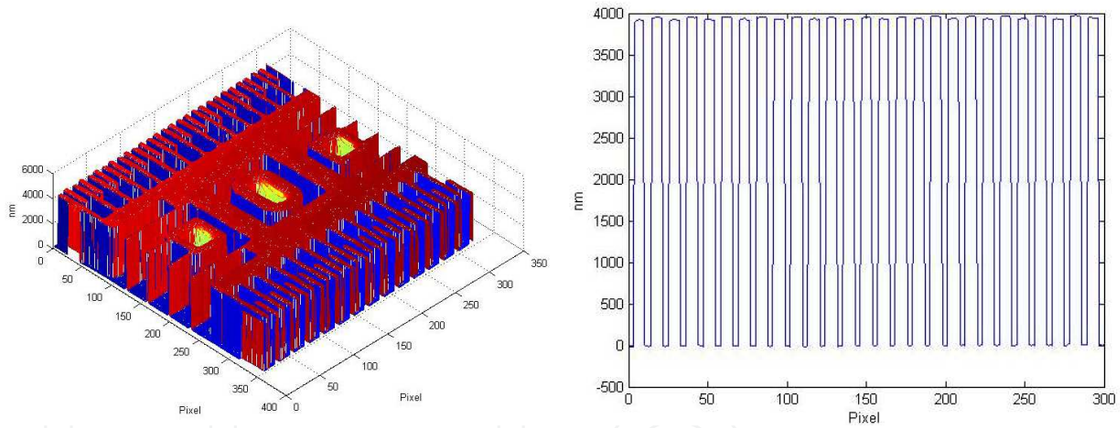

(a) 3D structure of the resonator (b) Comb-finger profile of the resonator

Fig. 17. Measurement of the resonator

4.5 Dynamic characterization

4.5.1 In-plane motion measurement

A 20× objective was used in the dynamic experiments. The stimulating signal was sine waveform with 10V amplitude, 20V offset voltage. The exposing time of CCD was 20ms for LED illumination and 100μs for LD illumination. The strobed pulse percent was 100%. The strobed phase number was 8 for in-plane motion measurement and 16 for out-of-plane motion measurement.

In order to get the resonant frequency of the tested device, the sweep-frequency measurement in a large range was firstly needed. The frequency increases in the logarithm mode, so the range of resonant frequency can be decided through one time frequency

sweeping measurement. Then another frequency sweeping measurement can be done in a small range. In summary, smaller range can achieve more times measurement, and the gotten resonant frequency will be more accurate. Figure 18 shows the experimental results in the range from 100 Hz to 100 kHz, the sweeping number is 21. After that, the frequency sweeping range can be decreased to 22 kHz~25 kHz, the sweeping number was 100 (see in figure 19). From that, the resonant frequency of the microstructure can be obtained. From the amplitude-frequency and phase-frequency curves, the device can be fitted into a second order system, the resonant frequency of the device is about 23.41 kHz, the maximum moving amplitude is around 764.52 nm, so the quality factor can be calculated as Q=23.41/(24.04-22.87)=20. Because of the air damp during the moving process of the device, the quality factor is not high. All data will be fed back to the designer and the quality factor of the device can be increased through improving the structure of the micro-resonator. Then five times of experiments without stimulating signal were done. The noise floor was calculated as 0.56 nm.

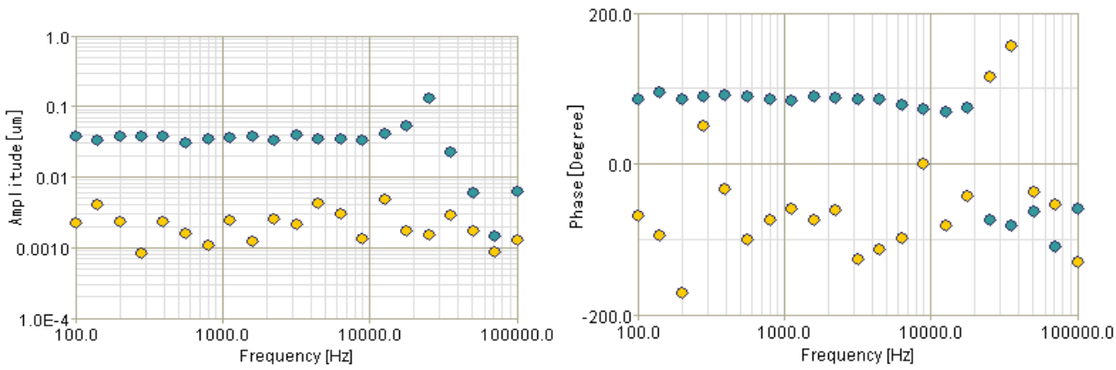

(a) Amplitude-frequency curve (b) Phase-frequency curve

Fig. 18. Large range sweep-frequency measurement of in-plane motion. The blue curve is the result in x direction. The yellow curve is the result in y direction.

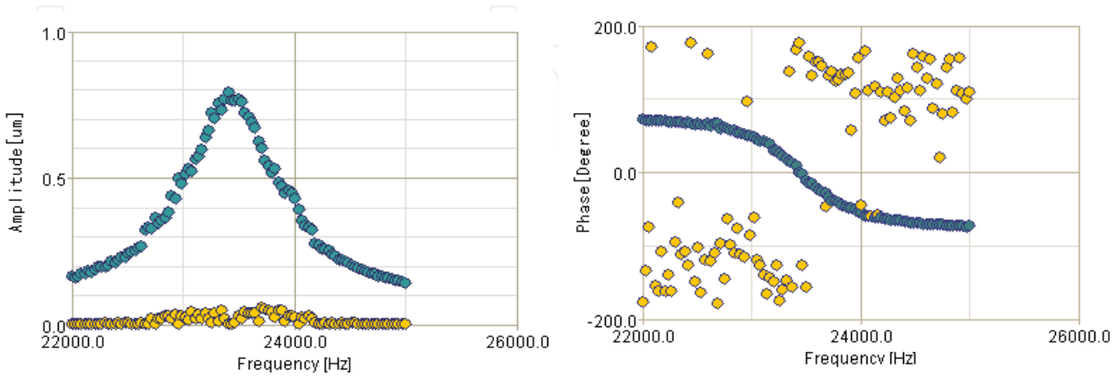

(a) Amplitude-frequency curve (b) Phase-frequency curve

Fig. 19. Small range sweep-frequency measurement of in-plane motion. The blue curve is the result in x direction. The yellow curve is the result in y direction.

In order to study the relationship between the stimulating voltage and the movement, amplitude sweeping experiments were performed. The stimulating frequency was 23 kHz with the starting amplitude 0% and the ending amplitude 100% (10 V). The sweeping number was 21 and the amplitude increased linearly. The experimental results were shown in figure 20. The curves show that the relationship between the moving amplitude and the stimulating voltage is linear which is consistent with the computer simulated results. It draws the conclusion that the design and fabrication process of the device are valid and the device has good dynamic behaviors.

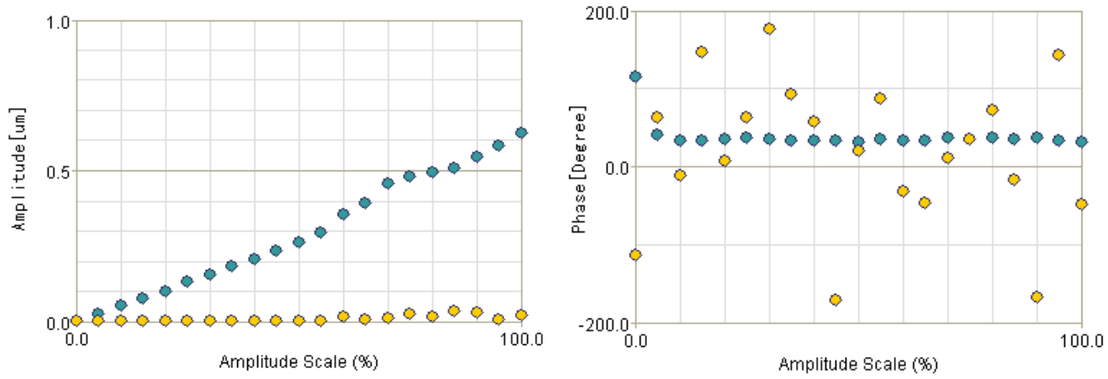

(a) Amplitude-scale curve (b) Phase-scale curve

Fig. 20. Sweep-amplitude measurement of in-plane motion. The blue curve is the result in x direction. The yellow curve is the result in y direction.

4.5.2 Dynamic profile measurement

A region of interest (ROI, see in figure 21) on the device was tested to study the dynamic profile change at a certain stimulating signal. The dynamic profiles were shown in figure 22.

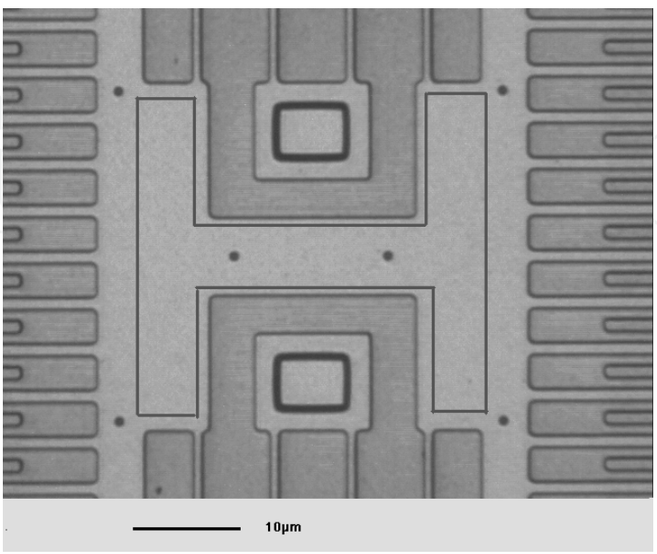

Fig. 21. Choice of ROI

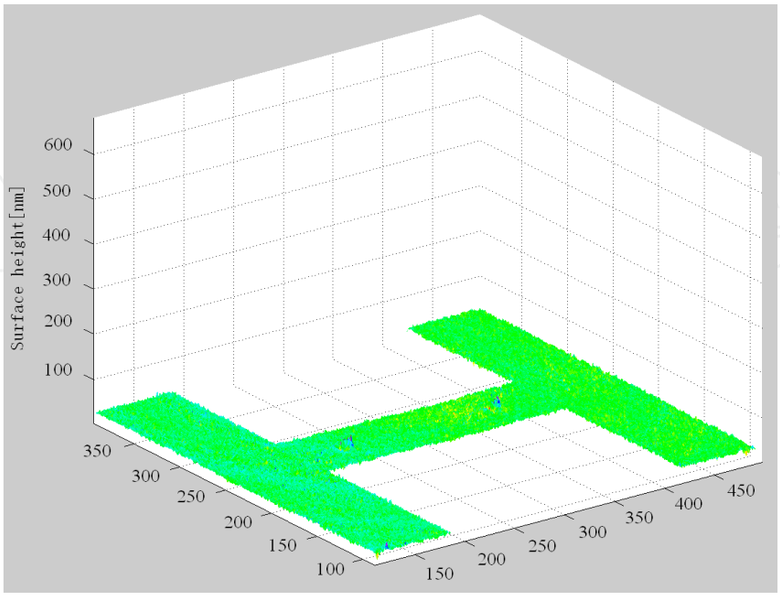

(a) Profile at the second phase

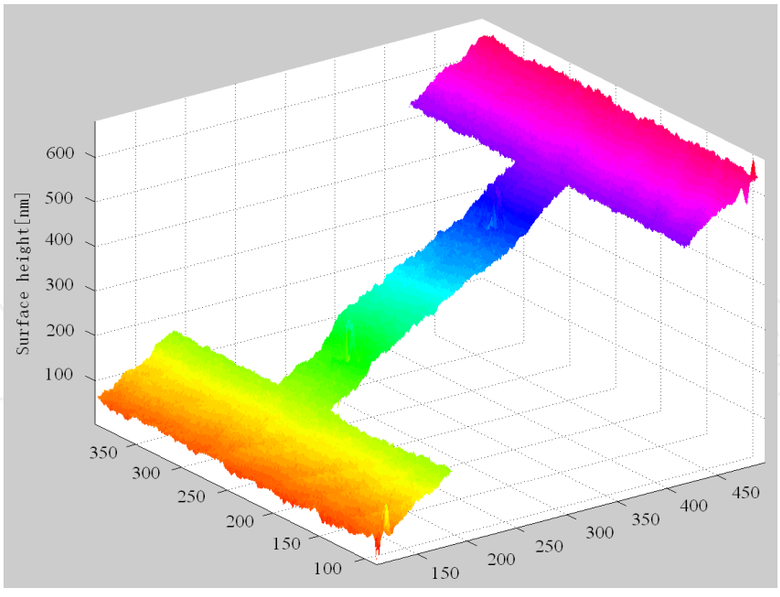

(b) Profile at the ninth phase

Fig. 22. Dynamic profile measurement

The stimulating voltage frequency was 23 kHz, the amplitude was 10 V, and the offset voltage was 20 V. The motion can be classified into three kinds of cases: 1) one reference plane; 2) the first phase of the device movement; 3) the reference mirror in the interferometer. Here the second case is chosen. From figure 22, it can be shown that the movement of the device is like sinusoidal waveform and there is a distort phenomena in the process of the movement.

5. Conclusion

This chapter has discussed several optical methods to realize MEMS characterization, including dimensional (static) and moving (dynamic) properties analysis. Two measuring systems are introduced. NMM based system combines nano-measuring machine with high positioning accuracy and microscopic interferometers. PSI, WLI, WLPSI are applied in the system to measure the dimensional parameters. MMA combines video microscopy, stroboscopic illumination and special algorithms. It employs two kinds of nondestructive methods - computer microvision for in-plane motion measurement and phase shifting interferometry for out-of-plane motion measurement. This system can test the three-dimensional motions and dynamic profiles with nanometer accuracy.

6. Acknowledgment

The authors gratefully acknowledge the support of National Natural Science Fund (91023022), International Cooperation Project of MOST (2008DFA71610) and Natural Science Fund of Tianjin (09JCYBJC05300).

7. References

Bosseboeuf, A., Gilles, J. P., Danaie, K. et al.(1999). A versatile microscopic profilometer-vibrometer for static and dynamic characterization of micromechanical devices. *Proc. SPIE*, Vol. 3825, pp. 123-133

Burdess, J. S., Harris, A. J., Wood, D. et al. (1997). A system for the dynamic characterization of microstructures. *J. Microelectromechan. Syst.*, Vol.6, No.4, pp. 322-328

Fu, X., Liu, Y. Q., Hu, X. D. et al. (2004). Micro Laser Doppler Vibrometer Technology for MEMS Dynamic Measurement. *J of Optoelectronics·Laser*, Vol.15, No.11, pp.1357-1360

Guo, T., Chang, H., Chen, J.P. et al. (2009). Micro-motion Analyzer used for Dynamic MEMS Characterization, *Optics and Lasers in Engineering*, Vol. 47, No.3-4, pp. 512-517

Guo, T., Wu, Z. C., Ma, L. et al.(2010). Dynamic MEMS characterization system using differential phase measurement method, *Proceedings of SPIE*, Vol. 7544, pp. 75444W

Guo, T., Ma, L., Zhao, J. et al. (2011). A nanomeasuring machine based white light tilt scanning interferometer for large scale optical array structure measurement, *Optics and Lasers in Engineering*, Vol. 49, No.9-10, pp.1124-1130

Guo, T., Ma, L., Chen, J.P. et al.(2011). MEMS surface characterization based on white light phase shifting interferometry, *Optical Engineering*, Vol. 50, No.5, pp. 053606

Hartzell, A. L., Woodilla, D. J. (2001). MEMS reliability, characterization, and test. *Proc. SPIE*, Vol. 4558, pp. 1-5

Ma, L., Guo, T., Yuan, F. et al.(2009). Thick film geometric parameters measurement by white light interferometry, *Proceedings of SPIE*, Vol. 7507, pp. 75070G

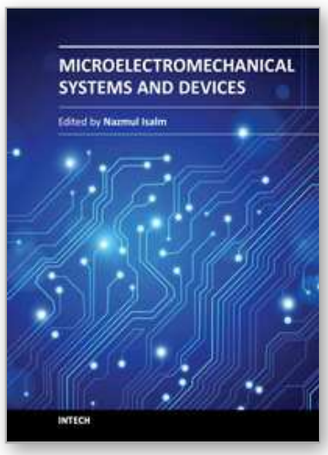

Microelectromechanical Systems and Devices

Edited by Dr Nazmul Islam

ISBN 978-953-51-0306-6
Hard cover, 480 pages
Publisher InTech
Published online 28, March, 2012
Published in print edition March, 2012

The advances of microelectromechanical systems (MEMS) and devices have been instrumental in the demonstration of new devices and applications, and even in the creation of new fields of research and development: bioMEMS, actuators, microfluidic devices, RF and optical MEMS. Experience indicates a need for MEMS book covering these materials as well as the most important process steps in bulk micro-machining and modeling. We are very pleased to present this book that contains 18 chapters, written by the experts in the field of MEMS. These chapters are groups into four broad sections of BioMEMS Devices, MEMS characterization and micromachining, RF and Optical MEMS, and MEMS based Actuators. The book starts with the emerging field of bioMEMS, including MEMS coil for retinal prostheses, DNA extraction by micro/bio-fluidics devices and acoustic biosensors. MEMS characterization, micromachining, macromodels, RF and Optical MEMS switches are discussed in next sections. The book concludes with the emphasis on MEMS based actuators.

INTECH
open science | open minds

InTech Europe
University Campus STeP Ri
Slavka Krautzeka 83/A
51000 Rijeka, Croatia
Phone: +385 (51) 770 447
Fax: +385 (51) 686 166
www.intechopen.com

InTech China
Unit 405, Office Block, Hotel Equatorial Shanghai
No.65, Yan An Road (West), Shanghai, 200040, China
中国上海市延安西路65号上海国际贵都大饭店办公楼405单元
Phone: +86-21-62489820
Fax: +86-21-62489821

IntechOpen